

Heating-Induced Transformations of Atmospheric Particles: Environmental Transmission Electron Microscopy Study

Daniel P. Veghte,[†] Swarup China,[†] Johannes Weis,^{‡,§} Peng Lin,^{||} Mallory L. Hinks,^{||} Libor Kovarik,[†] Sergey A. Nizkorodov,^{||} Mary K. Gilles,[‡] and Alexander Laskin^{*,†,||}

[†]William R. Wiley Environmental Molecular Sciences Laboratory, Pacific Northwest National Laboratory, Richland, Washington 99354, United States

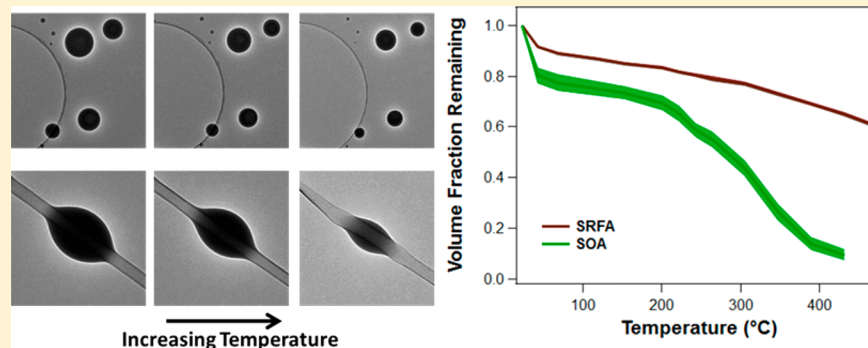
[‡]Department of Chemistry, University of California, Berkeley, California 94720, United States

[§]Chemical Sciences Division, Lawrence Berkeley National Laboratory, Berkeley, California 94720, United States

^{||}Department of Chemistry, University of California, Irvine, California 92697, United States

[†]Department of Chemistry, Purdue University, West Lafayette, Indiana 47907-2084 United States

Supporting Information



ABSTRACT: Environmental transmission electron microscopy was employed to probe transformations in the size, morphology, and composition of individual atmospheric particles as a function of temperature. Two different heating devices were used and calibrated in this work: a furnace heater and a Micro Electro Mechanical System heater. The temperature calibration used sublimation temperatures of NaCl, glucose, and ammonium sulfate particles, and the melting temperature of tin. Volatilization of Suwanee River Fulvic Acid was further used to validate the calibration up to 800 °C. The calibrated furnace holder was used to examine both laboratory-generated secondary organic aerosol particles and field-collected atmospheric particles. Chemical analysis by scanning transmission X-ray microscopy and near-edge fine-structure spectroscopy of the organic particles at different heating steps showed that above 300 °C particle volatilization was accompanied by charring. These methods were then applied to ambient particles collected in the central Amazon region. Distinct categories of particles differed in their volatilization response to heating. Spherical, more-viscous particles lost less volume during heating than particles that spread on the imaging substrate during impaction, due to either being liquid upon impaction or lower viscosity. This methodology illustrates a new analytical approach to accurately measure the volume fraction remaining for individually tracked atmospheric particles at elevated temperatures.

Primary and secondary organic aerosols (POA and SOA) contribute up to 90% of the submicron particle mass in most atmospheric environments.^{1,2} SOA, formed from the oxidation of biogenic volatile organic compounds (VOCs) emitted by trees, is the major source of condensed-phase organics in the atmosphere.^{3,4} POA includes direct emissions from fossil fuel combustion, biomass burning, and other natural sources such as soil organic material.^{5–7} Furthermore, organic matter with poorly described physical properties from marine biological activity is enhanced in submicron sea spray particles.^{8–10} Loss of the more volatile constituents from POA, followed by the atmospheric oxidation, also contributes to SOA formation.^{4,11} Additionally, SOA material forms coatings

on soot, mineral dust, and other refractory particles.^{12,13} Particle coatings by SOA material have important implications because they may increase the absorption of light by particles due to the lensing effect.^{13–15} Formation, growth, and aging of atmospheric particles depend strongly on the volatility and reactivity of gas and particle-phase components.¹⁶ For instance, SOA grows through condensation of organic compounds with low saturation vapor pressures formed through gas-phase oxidation of VOCs.^{3,4,17} For highly viscous, semisolid SOA

Received: March 29, 2018

Accepted: July 16, 2018

Published: July 16, 2018

particles, the time scale of diffusion through the particle may be longer than the time scale for VOC oxidation. This results in deviations from gas–particle partitioning equilibrium.^{18–20} Because of the lack of understanding of the rheological properties of aerosol particles, these effects are insufficiently incorporated in models.^{21,22} Additionally, as particles are transported from the source location, aging processes modify their chemical composition and physical properties.^{23,24} Characterizing volatilization of different types of organic particles is essential for predictive understanding of their effects on atmospheric chemistry and climate.

The volatility of organic compounds in particles can be studied while heating particles and measuring changes in particle size and the chemical composition of both gas and condensed phases. Traditionally, this has been done using thermal denuders where ensembles of airborne particles pass through a heated flow system prior to probing by an analytical chemistry technique.^{25,26} Thermal denuders have been most commonly used to study volatility of atmospheric organic compounds over temperature ranges of 100–400 °C.^{26,27} Different types of laboratory-generated SOA have been studied in detail, and literature reports concluded that laboratory-generated SOA proxies are frequently more volatile than field-collected SOA.^{26–28} Volatilization at ambient temperature for SOA particles can require hours to complete due to inherent transport limitations in viscous particles.^{29,30} SOA generated from various VOC precursors exhibit variability in their volatility. Specifically, for SOA formed from anthropogenic precursors such as OH oxidation of toluene and xylene, ~20% of their mass remains at 150 °C, while SOA from OH oxidation and ozonolysis of biogenic precursors, α -pinene and β -caryophyllene, completely volatilizes by 150 °C.²⁷ For field-collected biomass burning organic particles, approximately 20% of their mass remains at 200 °C while laboratory-generated SOA is almost completely volatilized at the same temperature.²⁶ Additionally, for atmospherically aged organic particles, although 75% of the mass evaporated after heating to 150 °C, no significant differences in composition were observed.³¹

Samples of atmospheric particles are complex mixtures of various chemical components with diverse internal and external mixing states that cannot be adequately probed by bulk- and ensemble-based techniques. Understanding their volatility is an experimental challenge that requires methods developed for individual particle analysis. Recent advancements in transmission electron microscopy (TEM) have allowed for in situ analysis of individual particles with nanometer resolution. TEM allows examination of the individual components in complex particle mixtures such as ensembles of field-collected aerosol samples.^{5,32–34} Heating experiments inside a TEM instrument can be performed under different gas atmospheres. Recent applications of in situ heating using TEM have included: nanoparticle aggregation on surfaces,³⁵ sintering of nanoparticles,³⁶ material atomic structural changes at high temperature,³⁷ nanowire growth on surfaces phase transitions,³⁸ sublimation of nanoparticles,³⁹ and volume changes of biomass burning aerosol particles.⁴⁰ However, temperature calibration on the sample is challenging because of the temperature is measured on the surrounding holder, not the sample itself. Novel methods to calibrate the temperature directly at the sample itself include: electron energy loss spectroscopy,⁴¹ vibrational spectroscopy,⁴² Raman thermometry,⁴³ and measuring lattice parameters of known

particle standards.⁴⁴ Because TEM is operated under vacuum, the most volatile components in a sample can be lost initially. In addition, there is the potential for electron-beam-induced damage to the remaining particle components.⁴⁵ Nevertheless, microscopic imaging with in situ heating provides unparalleled information about the volatility of individual particles within complex particle samples. Understanding the volatility of individual components in a heterogeneous particle mixture is essential for practical interpretation of particle optical properties measured by the ensemble based techniques, resulting in new applications toward modeling of atmospheric aerosol properties.

In this study, we employ two heating holder types [furnace and a Micro Electro Mechanical System (MEMS)] to probe the volatility of atmospherically relevant organic particles. Previously, furnace holders have been used to study heat-induced transformations of biomass burning airborne particles.⁴⁰ However, systematic comparison and calibration of furnace holders with MEMS devices using standard reference materials have not been reported. Here, we use sublimation temperatures of NaCl, glucose, and ammonium sulfate particles along with the melting point of tin as standards to conduct systematic corrections of both heating devices. This calibration is further validated using the volatilization of Suwannee River Fulvic Acid (SRFA) for temperatures up to 800 °C. We also present a method to determine the volume fraction remaining for SOA particles. We then apply this technique to determine the difference in volume fraction remaining of field-collected particles from the Amazon.

METHODS

Particle Generation. Particle standards for heating were generated through either nebulization of an aqueous solution and drying the particles (NaCl, AS, SRFA) before being impacted onto microscopy substrates or dry generated (glucose, tin) by dispersing a small quantity on the substrate and excess blown off by dry nitrogen. SOA were produced using a custom-built OH oxidation flow reactor from VOC precursor vapor (Figure S1). Field samples of atmospheric particles were collected north of Manaus, Brazil during the GOAMAZON campaign on stage 8 of a MOUDI impactor.⁴⁶ Additional sampling information and Hybrid Single-Particle Lagrangian Integrated Trajectory (HYSPPLIT) model⁴⁷ trajectories (Figure S2) can be found in the Supporting Information.

Heating Experiments in the ETEM. Samples were imaged in an FEI Titan Environmental Transmission Electron Microscope (ETEM) operated at 300 kV. For imaging beam sensitive ammonium sulfate (AS) particles a low dose imaging approach was employed. The low dose imaging uses low electron flux in combination with a direct electron detector (Direct Electron, Inc.).⁴⁸ AS particles, which usually show visible damage after a few seconds of electron beam exposure, exhibited no morphological changes after 15 min under low dose imaging conditions (Figure S3).⁴⁵ Particles were additionally imaged by scanning electron microscopy (SEM; Quanta 3D, FEI, Hillsboro, OR) operated at 20 kV. Images were obtained at a 75° tilt angle perpendicular to the electron beam.

For heating particles, two separate sample holders were employed: a MEMS device and a furnace holder. The furnace double tilt heating holder (Gatan, model 652) is compatible with standard 3 mm TEM grids. To minimize the effects of major temperature gradients, particles located near the edge of

the TEM grid (within 3 grid cells of the edge) were imaged. The MEMS method used individually calibrated substrates with a resistively heated silicon carbide membrane with a 7×7 array containing $7 \mu\text{m}$ diameter holes coated with holey carbon in the open loop mode (Aduro, Protochips, Inc.). In these experiments, particles as close to the center of the MEMS chip as possible were imaged where the temperature gradient is the smallest. In experiments, the furnace holder and MEMS were heated to the desired temperature and held for 5 min prior to cooling to room temperature for imaging. The MEMS device was heated at a rate of $2 \text{ }^\circ\text{C/s}$, while the furnace holder was heated between $0.04 \text{ }^\circ\text{C/s}$ to $7.73 \text{ }^\circ\text{C/s}$ with an increasing rate with temperature (Figure S4). Individual particle volume was calculated on the basis of the projected area from the ETEM images as discussed in the Supporting Information and Figures S5 and S6.

Chemical Characterization of Particle Samples after Heating. Bulk heating of the particle samples was performed using a tube furnace (MTI GSL 1300X). For the high-resolution mass spectrometry (HRMS) measurements, separate SRFA particle samples impacted on the aluminum foils were heated to 150, 300, or $400 \text{ }^\circ\text{C}$. For scanning transmission X-ray microscopy near-edge X-ray fine structure (STXM/NEXAFS), the SRFA and toluene SOA samples impacted on the silicon nitride windows were heated to 150 or $350 \text{ }^\circ\text{C}$. The tube furnace was kept under a dry nitrogen atmosphere and samples were heated at $20 \text{ }^\circ\text{C/min}$, held at the target temperature for 5 min, and then cooled to room temperature at $20 \text{ }^\circ\text{C/min}$. SRFA samples were analyzed using an LTQ-Orbitrap ESI-HRMS (Thermo Fisher Scientific). STXM/NEXAFS was used to acquire the carbon (278–320 eV) and oxygen (525–550 eV) K-edge spectra of individual particles^{49–51} before and after heating. Additional instrumentation details can be found in the Supporting Information.

RESULTS AND DISCUSSION

Calibration of the Temperature Response of the Heating Holders. Figure 1 shows schematics of the furnace

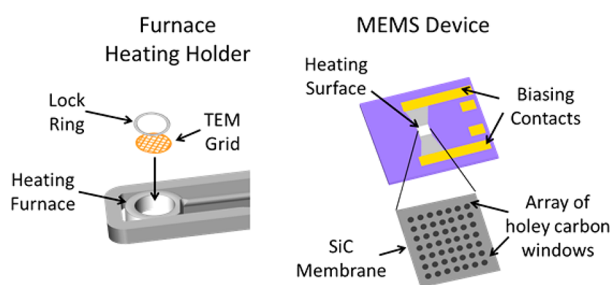


Figure 1. Schematics of the furnace heating holder (left panel) designed to work with standard TEM grids and the MEMS device (right panel) heated through applying a bias to the contacts attached to the silicon carbide (SiC) heating membrane.

and the MEMS heating holders employed in this study. Furnace holders rely on temperature control over the surrounding support ring, rather than direct temperature measured at the substrate surface. In the MEMS system, the substrate itself is a miniature silicon carbide precalibrated heating element, where the temperature of the substrate is controlled with precision better than $0.1 \text{ }^\circ\text{C}$. For the MEMS microchips, each substrate has a uniform heating gradient with variations of only a few $^\circ\text{C}$ across the silicon carbide substrate

membrane and can heat with rates up to $1000 \text{ }^\circ\text{C/s}$ to temperatures above $1100 \text{ }^\circ\text{C}$.⁵² The furnace heating holder can be heated up to $800 \text{ }^\circ\text{C}$, with the heating rate dependent on the desired temperature. However, the MEMS approach also has certain caveats such as limited types of substrates, lower total area for particle analysis, and the system and substrates are substantially more expensive. Although Cu grids are routinely used in TEM experiments, previously it was reported that when heated above $600 \text{ }^\circ\text{C}$ copper migrates and forms Cu nanoparticles which hinder particle analysis.⁵³ This phenomena of Cu nanoparticle formation was confirmed by heating blank Cu grids to a $600 \text{ }^\circ\text{C}$. A similar test with Mo grids, heated up to $800 \text{ }^\circ\text{C}$ showed no evidence of nanoparticle formation. Therefore, Mo grids were selected for use in our experiments.

Glucose, AS, tin, and NaCl particles were used to compare the set temperature conditions of the two heating holders. The melting point of tin is $232 \text{ }^\circ\text{C}$,⁵⁴ and the calculated sublimation temperature at 5×10^{-6} mbar for glucose is $111 \text{ }^\circ\text{C}$ ⁵⁵ and that for NaCl is $448 \text{ }^\circ\text{C}$ ⁵⁶ at 5×10^{-6} mbar. Figure 2 shows examples of the phase changes observed for each species using the MEMS holders. A full discussion of the observed changes can be found in the Supporting Information. Glucose was observed to evaporate at a set point of $120 \text{ }^\circ\text{C}$ in the furnace holder and at $160 \text{ }^\circ\text{C}$ in the MEMS holder. After the initial loss of particles mass, AS sublimed at a set point of $120 \text{ }^\circ\text{C}$ using the furnace holder and $180 \text{ }^\circ\text{C}$ using the MEMS holder. The melting point for tin was observed at a set point of $230 \text{ }^\circ\text{C}$ for both the furnace and MEMS holders. NaCl sublimed at a set point of $570 \text{ }^\circ\text{C}$ in the furnace holder and $440 \text{ }^\circ\text{C}$ in the MEMS holder. Additional images and analysis can be found in the Supporting Information (Figures S7 and S8). For the SRFA particles, there was a gradual loss of particles in both the furnace and MEMS holders (Figure S9) with material remaining up to $1100 \text{ }^\circ\text{C}$ (Figure S10). Figure 3 shows a correlation plot between set temperatures of the furnace and the MEMS experiments. The individual data points correspond to the set temperatures where analogous physical changes were imaged for glucose, NaCl, tin, AS, and SRFA particles. The experimental points for glucose, NaCl, and AS particles correspond to complete sublimation from the substrate. The point for tin corresponds to the temperature at which the particles melted and changed from an irregular shape to a spherical morphology. For SRFA, the data point corresponds to the set temperatures where the calculated volume equivalent diameters were equal between the furnace and MEMS experiments. Below $200 \text{ }^\circ\text{C}$, the furnace temperature is consistent with reported phase changes, while the MEMS heater requires a higher temperature to observe similar phase changes. At temperatures around $220 \text{ }^\circ\text{C}$, both the furnace and MEMS heaters observe phase changes at the same temperatures. Above $250 \text{ }^\circ\text{C}$, the furnace holder requires increasingly higher temperature to observe the same changes seen with the MEMS heater. Using the particle sublimation points NaCl, the melting point of tin, and the correlated similar fractional volume loss of SRFA at the $800 \text{ }^\circ\text{C}$, the furnace holder temperature between 230 and $800 \text{ }^\circ\text{C}$ was corrected according to

$$T_{\text{MEMS}}^{230-800^\circ\text{C}} = 0.38 \times T_{\text{furnace}} + 161.37$$

This correction is for this specific furnace holder used in our study and could vary for individual heating holders. Correction of the furnace holder showed that at the set point of $800 \text{ }^\circ\text{C}$,

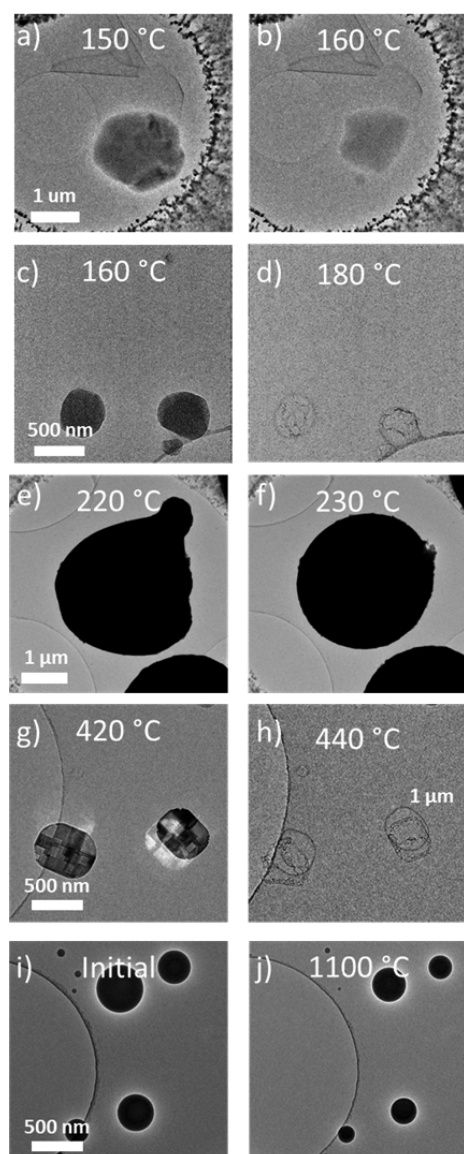


Figure 2. ETEM images of (a,b) glucose, (c,d) ammonium sulfate (AS), (e,f) tin, and (g,h) NaCl just prior to and after observed phase change using the MEMS heating holder. (i, j) SRFA particles initially and heated to highest temperature.

the corrected temperature of the grid is only around 440 °C. Figure 3 compares the heating curve of SRFA in using the MEMS device with the calibrated experiments for the furnace holder. There is good agreement between the calibrated SRFA data from the furnace holder and that found using the MEMS device. Experiments using standards demonstrated the furnace holder was well calibrated below 230 °C but needed additional corrections at higher temperatures. At high temperatures, there is substantial heat loss from the heating ring of the furnace holder leading to a lower temperature on the substrate than measured by the thermocouple attached to the ring. The MEMS heater worked well above 200 °C where there is a linear response of temperature to current, but at lower temperatures, nonlinearity in the current-temperature response led to less accurate temperature settings.⁴² After temperature corrections at temperatures above 230 °C, the furnace holder can be used to compare the heating behavior of different

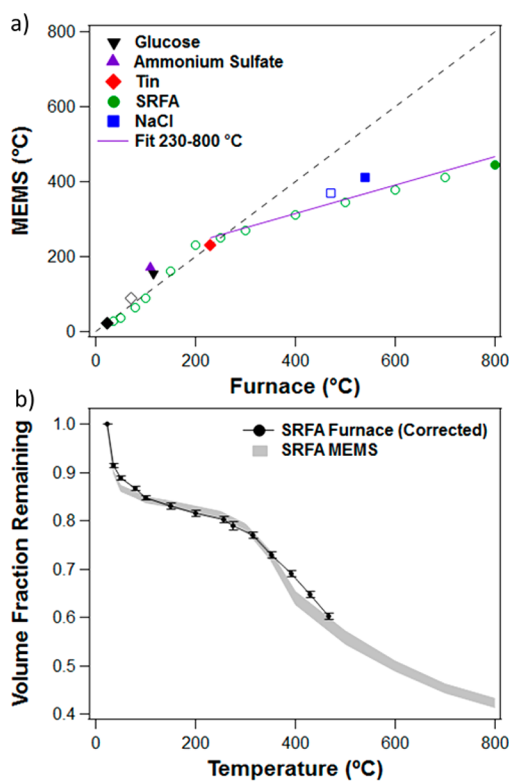


Figure 3. (a) Correlation of the set temperatures between the furnace holder and MEMS device at which the same physical changes occurred in glucose, AS, NaCl, and SRFA particles. The solid points are used for correction, while the open points demonstrate the intermediate stages. The dashed line corresponds to a 1:1 correlation. (b) Volume fraction remaining of SRFA particles measured in the MEMS and the furnace experiments, for which sample temperature was determined using corrections above 230 °C shown in the upper panel. The error bars denote the standard error.

particle types present in atmospheric samples over a large temperature range.

Volatilization of SOA Particles. Generally, all three types of SOA particles had similar trends in their volume loss as illustrated by Figure 4m. *ben*-SOA particles have the highest fraction of material remaining after heating compared to *xyl*-SOA and *tol*-SOA, which show similar remaining fractions. Approximately 20% of the volume is lost when the temperature is increased above 35 °C. After that, *ben*-SOA and *tol*-SOA particles gradually shrink to an approximately 60% volume fraction at 300 °C, while *xyl*-SOA particles remain fairly consistent over the same temperature range. After heating above 300 °C, *xyl*-SOA and *tol*-SOA particles rapidly decrease in volume, and at 350 °C only 10% of the volume remains. *ben*-SOA particles exhibit a slower decrease in volume and almost 20% of their volume remains at 350 °C. Only minor differences in volume loss were observed for *ben*-SOA particles heated in the presence of 1 mbar of N₂ compared to high vacuum (10⁻⁶ mbar) conditions (Figure S11 and S12). Chemical imaging of particles from all three SOA types by STXM/NEXAFS show comparable chemical composition as indicated by the similar spectral features shown in Figure S13. Previous studies suggested that the main mechanisms for volatilization was thermal degradation of oligomers where independent of the VOC precursors, SOA would show similar behavior at high temperatures.²⁷ Specifically, the volatilization of SOA using thermal denuder techniques has shown that more than 50% of

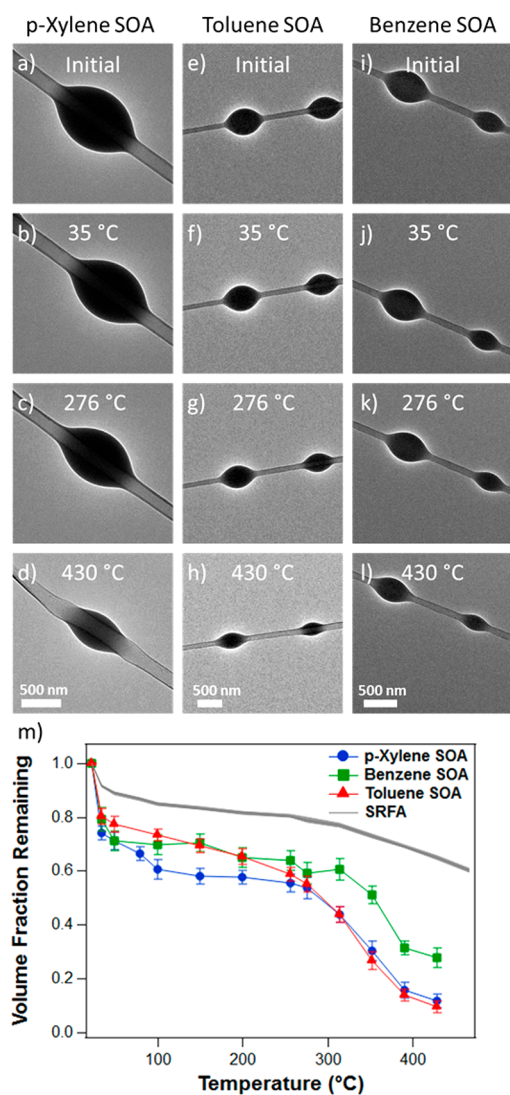


Figure 4. (a–l) ETEM images of laboratory-generated SOA particles heated up to 430 °C using the furnace holder. (m) Volume fraction remaining of SOA and SRFA particles as a function of temperature. Temperatures are corrected values reached by the heating devices. Error bars are the standard error of the measurements.

the particle volume is lost by 100 °C with a residence time in the thermal denuder of ~ 12 s.^{26–28} These experiments analyzed the volatility of SOA particles immediately after generation. In our experiments, the collected particles were kept at ambient conditions for some time (\sim days) before analysis, so the most volatile components were likely lost either prior to analysis or when exposed to high vacuum conditions. In the atmosphere, gas-particle equilibrium may require hours or days with a considerable amount of the material becoming nonvolatile under standard atmospheric conditions.³⁰ Heating experiments of individual SOA particles in the ETEM showed the volume fraction remaining after heating up to 300 °C was still considerable, while rapid loss of material occurred only above 350 °C.

Chemical Imaging of SRFA and SOA Changes after Heating. The chemical composition of SRFA and SOA particles before and after heating experiments was analyzed using STXM/NEXAFS and ESI-HRMS. Figure 5a shows the NEXAFS carbon K-edge spectra of SRFA particles before heating, heated to 150 and 350 °C, respectively. The spectra

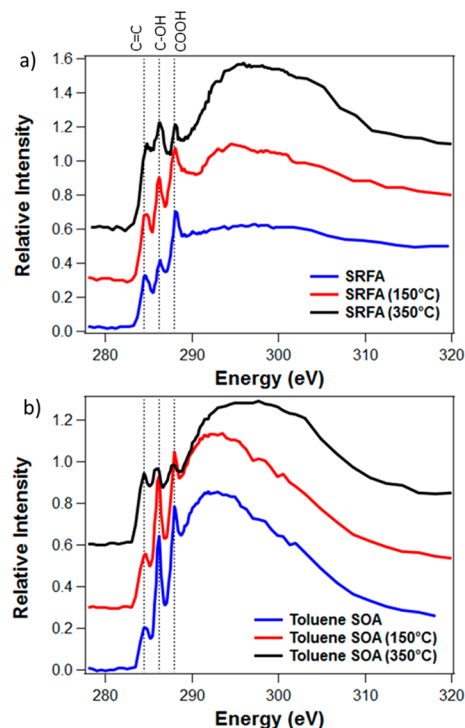


Figure 5. STXM/NEXAFS spectra of (a) SRFA and (b) *tol*-SOA particles before and after heating to 150 and 350 °C where charring of the particles starts to occur. The spectra are normalized to the post edge and offset for clarity.

show substantial evolution in the relative abundances of C=C (284.5 eV), C–OH (286.1 eV), and COOH (288 eV) peaks after the heating experiments. When heated to 150 °C, there was no substantial change observed with only minor increase in the C–OH peak. Further heating to 350 °C resulted in significant decrease in the COOH peak simultaneously with an increase in the sp^2 peak, indicative of charring. Previous literature reports have shown that initial charring of organic matter occurs above 300 °C, and its composition continues to evolve approaching graphite-like structures at 2000 °C.^{57,58} Consistently, in our previous work, we showed that when heating organic components to 350 °C, they become highly absorbing as a consequence of charring of the organic component.⁵⁹ ESI-HRMS data included in Figure S14 also showed a trend similar to the NEXAFS observations. The HRMS spectra of the SRFA particle samples compared to those heated to 150 °C show that there is a loss of the low molecular weight species with m/z values under 250. The ESI-HRMS of the SRFA particles heated to 300 °C shows only a small number of ionizable components present in the sample, which is consistent with the carbonization (charring) upon heating. After heating to 400 °C, virtually no peaks were detected by ESI-HRMS analysis, while a few background peaks observed in the spectra were related to impurities of the collection substrate. This loss of any discernible peaks in the ESI-HRMS spectra of SRFA material heated above 300 °C is consistent with charring, where carbonized components are not susceptible to ESI ionization. NEXAFS and HRMS demonstrated that when SRFA particles were heated to 150 °C, there was a change in the molecular composition of the organics, and with additional heating above 350 °C, the remaining carbonaceous components began to char, becoming nonvolatile.

The compositions of *tol*-SOA particles heated to 150 and 350 °C were compared to the initial material to probe compositional changes at each temperature. Figure 5b shows the STXM/NEXAFS spectra of *tol*-SOA particles before and after heating to 150 and 350 °C, respectively. The spectra are fairly similar before and after heating to 150 °C, with the latter indicating only a slight increase in the sp^2 carbon peak. However, a substantial difference is observed for particles heated to 350 °C, where a significant decrease in the oxygenated carbon peaks (C–OH and COOH), and an increase in the sp^2 carbon peak were observed. Analysis of the O:C ratio further confirmed the decrease in the oxygen content from the initial value of 1.57 ± 0.38 to 1.12 ± 0.17 at 150 °C and below the detection limit at 350 °C. These observations are consistent with the commonly observed charring trend of organic species^{57,58} and the SRFA data discussed above.

Volatilization of Field-Collected Particles. Field samples of atmospheric particles collected above the canopy of the Amazon tropical forest exhibited multiple types of organic particles, ranging from highly viscous particles (no adhesion to the lacy carbon film) to low viscosity where the particles bead up on the thin film strands. The back trajectories of the air mass arriving at the sampling site are shown in Figure S2 and indicate long northeast transport to the site from the forested areas without the influence of major anthropogenic sources. The particles were collected at the beginning of February, which is the wet season in the Amazon, which suggests that the particles are primarily from local biogenic sources. Figure 6 shows an example of three particle types during heating experiments up to 390 °C in the furnace holder: (a–c) a spherical highly viscous (glassy-like) particle, (d–f) a particle with low viscosity that adheres to the thin strand of the film, and (g–i) a low-viscosity particle beaded up around the thin strand of the film with an inclusion that is damaged and removed below 200 °C, which is presumably ammonium sulfate. For all three cases, some organic material remains on the substrate even at the highest temperature, but for the lower-viscosity particles almost no sample residual remains. Figure 6j shows the average volume fraction remaining for each particle type during heating up to 390 °C. For both high and low-viscosity particles at 35 °C there is an initial loss of ~10% of the volume fraction. Above 35 °C the spherical particles (high viscosity) shrink gradually, while low-viscosity particles lose more volume when heated to 50 °C and remain at 70–75% of their original volume at temperatures up to 250 °C. On average, for both particle types, a further decrease in the volume fraction remaining occurs above 250 °C, which then levels out as the temperature reaches 400 °C. Overall, the volume fraction remaining of the low-viscosity particles from the field sample is higher than those of the laboratory SOA particles. These observations are consistent with previous literature reports indicating that overall ambient organic particles are less volatile than those generated in laboratory experiments. These observations are consistent with previous literature reports indicating that overall ambient SOA particles are less volatile than laboratory-generated particles.^{26,27} For example, typical biomass burning organic particles had 60% mass fraction remaining after 200 °C.²⁶ The overall trends are similar to previous reports of heating experiments in TEM, where particles collected during biomass burning events showed approximately 60% and 20% of the remaining volume at 200 and 600 °C, respectively.⁴⁰ These field studies of

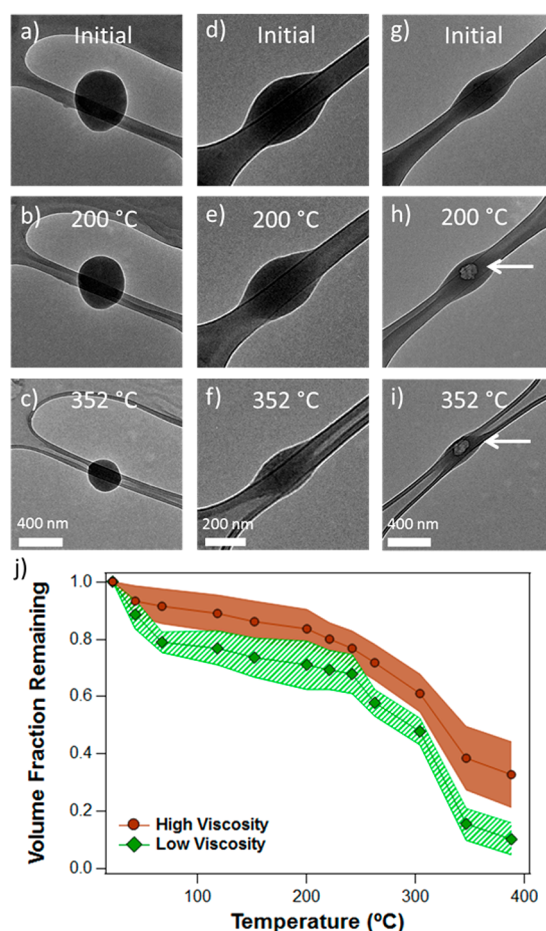


Figure 6. ETEM images of ambient organic particles collected over the tropical forest in the Amazon heated in the furnace holder: (a–c) a highly viscous glassy-like particle, (d–f) a low-viscosity particle with adhesion to the substrate, (g–i) a low-viscosity particle adhered to the thin strand of the substrate with inclusion noted by arrow. (j) Volume fractions remaining of high- (a) and low-viscosity (d) ambient organic particle types heated to 390 °C in the furnace holder. The standard error for the high-viscosity particles is shown by the shaded region and the low viscosity by the patterned region. Temperatures are corrected using the calibration established here.

ambient SOA using a thermal denuder were in good agreement with our ETEM heating experiments; whereas the thermal denuder experiments of freshly generated laboratory SOA had a higher volatility.^{26–28} This method shows that by examining individual particles, the volatility of different categories of particles can be distinguished within complex mixtures.

CONCLUSIONS

ETEM imaging of particles in heating experiments were used to probe the relative volatility of individual organic particles of atmospheric relevance. The furnace holder is demonstrated to be well suited for analysis of particles at temperatures under 230 °C, but requires accurate calibration at higher temperatures. Here, we presented the method of using a MEMS heater and employing standards for calibration. The particle composition before and after heating was probed by complementary STXM/NEXAFS and HRMS. Both methods detected molecular transformations indicative of charring above 350 °C. More than 70% of the volume fraction of SOA particles remained at 100 °C, followed by a relatively

modest decrease in particle volume up to temperatures of approximately 300 °C. Above 300 °C there was quick decrease in particle size with only 10–20% volume fraction remaining by 400 °C. When heating in above 300 °C, this increase in the loss of organic material was due to charring. Experiments were performed at pressures up to 10 mbar, with slight differences observed for the high volatility SRFA and SOA. The behavior of organic particles is different if heated in the presence of oxygen where additional loss of material was observed at temperatures above 250 °C. Samples of ambient particles from the Amazon were analyzed to determine the difference in volatility for the different particle types in a field sample. We observed that spherical type particles were less volatile than particles that spread over the substrate. Ambient organic particles collected in the Amazon tropical forest showed that solid high-viscosity particles retained nearly 30% of their volume at 400 °C, while less-viscous particles had less than 10% volume fraction remaining at the same temperature. The charring effects of organic particles at high temperatures may affect interpretation of data obtained by aerosol measurement techniques which employ thermal vaporization of particles. Additionally, humic-like compounds, such as SRFA, still contain material that does not vaporized even at temperatures up to 1100 °C. With this remaining material, there can be an underestimation of the mass and composition of organic aerosol. Therefore, probing volatility of individual particles is important for predictive understanding of transformations of different types of complex atmospheric particles in field-collected samples.

■ ASSOCIATED CONTENT

■ Supporting Information

The Supporting Information is available free of charge on the ACS Publications website at DOI: [10.1021/acs.analchem.8b01410](https://doi.org/10.1021/acs.analchem.8b01410).

Additional details including the setup to generate aerosol particles, the imaging of ammonium sulfate particles under low dose electron imaging, TEM images of SRFA particles heated under low vacuum and oxygen rich atmosphere, graph comparing high vacuum and low vacuum conditions for SRFA and SOA particles, HRMS of SRFA before and after heating, tilted SEM images of SOA and SRFA particles, and STXM/NEXAFS spectra of SOA particles (PDF)

■ AUTHOR INFORMATION

Corresponding Author

*E-mail: alaskin@purdue.edu.

ORCID

Swarup China: [0000-0001-7670-335X](https://orcid.org/0000-0001-7670-335X)

Sergey A. Nizkorodov: [0000-0003-0891-0052](https://orcid.org/0000-0003-0891-0052)

Alexander Laskin: [0000-0002-7836-8417](https://orcid.org/0000-0002-7836-8417)

Notes

The authors declare no competing financial interest.

■ ACKNOWLEDGMENTS

The Pacific Northwest National Laboratory (PNNL) group acknowledges support from the Science Acceleration Project of the Environmental Molecular Sciences Laboratory (EMSL). The Lawrence Berkeley National Laboratory (LBNL) group and A.L. acknowledge support from the U.S. Department of

Energy's Atmospheric System Research Program, an Office of Science, Office of Biological and Environmental Research (OBER). J. W. acknowledges the student exchange program between the University of Würzburg and U. C. Berkeley (curator Professor A. Forchel, Würzburg and NSF IGERT program at UCB, DGE-0333455, Nanoscale Science and Engineering - From Building Blocks to Functional Systems.) The HRMS, SEM, and ETEM analyses were performed at EMSL, a National Scientific User Facility sponsored by OBER at PNNL. PNNL is operated by the U.S. Department of Energy by Battelle Memorial Institute under contract DE-AC06-76RLO. We would like to thank D. Perea at PNNL for use of the tube furnace. STXM/NEXAFS analysis at beamlines 5.3.2.2 and 11.0.2.2 of the Advanced Light Source at LBNL is supported by the Director, Office of Science, Office of Basic Energy Sciences of the U.S. Department of Energy under Contract No. DE-AC02-05CH11231.

■ REFERENCES

- (1) Kanakidou, M.; Seinfeld, J. H.; Pandis, S. N.; Barnes, I.; Dentener, F. J.; Facchini, M. C.; Van Dingenen, R.; Ervens, B.; Nenes, A.; Nielsen, C. J.; Swietlicki, E.; Putaud, J. P.; Balkanski, Y.; Fuzzi, S.; Horth, J.; Moortgat, G. K.; Winterhalter, R.; Myhre, C. E. L.; Tsigaridis, K.; Vignati, E.; et al. *Atmos. Chem. Phys.* **2005**, *5*, 1053–1123.
- (2) Zhang, Q.; Jimenez, J. L.; Canagaratna, M.; Allan, J. D.; Coe, H.; Ulbrich, I. M.; Alfarra, M. R.; Takami, A.; Middlebrook, A. M.; Sun, Y. L.; Dzepina, K.; Dunlea, E.; Docherty, K. S.; DeCarlo, P. F.; Salcedo, D.; Onasch, T. B.; Jayne, J. T.; Miyoshi, T.; Shimojo, A.; Hatakeyama, S.; et al. *Geophys. Res. Lett.* **2007**, *34*, L13801.
- (3) Shrivastava, M.; Cappa, C. D.; Fan, J.; Goldstein, A. H.; Guenther, A. B.; Jimenez, J. L.; Kuang, C.; Laskin, A.; Martin, S. T.; Ng, N. L.; Petaja, T.; Pierce, J. R.; Rasch, P.; Roldin, P.; Seinfeld, J. H.; Shilling, J.; Smith, J. N.; Thornton, J. A.; Volkamer, R.; Wang, J.; et al. *Rev. Geophys.* **2017**, *55*, 509–559.
- (4) Robinson, A. L.; Donahue, N. M.; Shrivastava, M.; Weitkamp, E. A.; Sage, A. M.; Grieshop, A. P.; Lane, T. E.; Pierce, J. R.; Pandis, S. N. *Science* **2007**, *315*, 1259–1262.
- (5) Pósfai, M.; Gelencser, A.; Simonics, R.; Arato, K.; Li, J.; Hobbs, P. V.; Buseck, P. R. *J. Geophys. Res.* **2004**, *109*, D06213.
- (6) Wang, B.; Harder, T. H.; Kelly, S. T.; Piens, D. S.; China, S.; Kovarik, L.; Keiluweit, M.; Arey, B. W.; Gilles, M. K.; Laskin, A. *Nat. Geosci.* **2016**, *9*, 433–437.
- (7) Liu, L.; Kong, S.; Zhang, Y.; Wang, Y.; Xu, L.; Yan, Q.; Lingaswamy, A. P.; Shi, Z.; Lv, S.; Niu, H.; Shao, L.; Hu, M.; Zhang, D.; Chen, J.; Zhang, X.; Li, W. *Sci. Rep.* **2017**, *7*, 5047.
- (8) Prather, K. A.; Bertram, T. H.; Grassian, V. H.; Deane, G. B.; Stokes, M. D.; DeMott, P. J.; Aluwihare, L. I.; Palenik, B. P.; Azam, F.; Seinfeld, J. H.; Moffet, R. C.; Molina, M. J.; Cappa, C. D.; Geiger, F. M.; Roberts, G. C.; Russell, L. M.; Ault, A. P.; Baltusaitis, J.; Collins, D. B.; Corrigan, C. E.; et al. *Proc. Natl. Acad. Sci. U. S. A.* **2013**, *110*, 7550–7555.
- (9) O'Dowd, C. D.; Facchini, M. C.; Cavalli, F.; Ceburnis, D.; Mircea, M.; Decesari, S.; Fuzzi, S.; Yoon, Y. J.; Putaud, J.-P. *Nature* **2004**, *431*, 676–680.
- (10) Quinn, P. K.; Bates, T. S.; Schulz, K. S.; Coffman, D. J.; Frossard, A. A.; Russell, L. M.; Keene, W. C.; Kieber, D. J. *Nat. Geosci.* **2014**, *7*, 228–232.
- (11) Chan, A. W. H.; Isaacman, G.; Wilson, K. R.; Worton, D. R.; Ruehl, C. R.; Nah, T.; Gentner, D. R.; Dallmann, T. R.; Kirchstetter, T. W.; Harley, R. A.; Gilman, J. B.; Kuster, W. C.; de Gouw, J. A.; Offenberg, J. H.; Kleindienst, T. E.; Lin, Y. H.; Rubitschun, C. L.; Surratt, J. D.; Hayes, P. L.; Jimenez, J. L.; Goldstein, A. H. *J. Geophys. Res. Atmos.* **2013**, *118*, 6783–6796.
- (12) Adachi, K.; Buseck, P. R. *J. Geophys. Res. - Atmos.* **2013**, *118*, 3723–3730.

- (13) Liu, S.; Aiken, A. C.; Gorkowski, K.; Dubey, M. K.; Cappa, C. D.; Williams, L. R.; Herndon, S. C.; Massoli, P.; Fortner, E. C.; Chhabra, P. S.; Brooks, W. A.; Onasch, T. B.; Jayne, J. T.; Worsnop, D. R.; China, S.; Sharma, N.; Mazzoleni, C.; Xu, L.; Ng, N. L.; Liu, D.; et al. *Nat. Commun.* **2015**, *6*, 8435.
- (14) Saleh, R.; Marks, M.; Heo, J.; Adams, P. J.; Donahue, N. M.; Robinson, A. L. *J. Geophys. Res. Atmos.* **2015**, *120*, 10285–10296.
- (15) Cappa, C. D.; Onasch, T. B.; Massoli, P.; Worsnop, D. R.; Bates, T. S.; Cross, E. S.; Davidovits, P.; Hakala, J.; Hayden, K. L.; Jobson, B. T.; Kolesar, K. R.; Lack, D.; Lerner, B. M.; Li, S.-M.; Mellon, D.; Nuaaman, I.; Olfert, J. S.; Petaja, T.; Quinn, P. K.; Song, C.; et al. *Science* **2012**, *337*, 1078–1081.
- (16) Zhang, H.; Worton, D. R.; Shen, S.; Nah, T.; Isaacman-VanWertz, G.; Wilson, K. R.; Goldstein, A. H. *Environ. Sci. Technol.* **2015**, *49*, 9768–9777.
- (17) Jimenez, J. L.; Canagaratna, M.; Donahue, N. M.; Prevot, A. S. H.; Zhang, Q.; Kroll, J. H.; DeCarlo, P. F.; Allan, J. D.; Coe, H.; Ng, N. L.; Aiken, A. C.; Docherty, K. S.; Ulbrich, I. M.; Grieshop, A. P.; Robinson, A. L.; Duplissy, J.; Smith, J. D.; Wilson, K. R.; Lanz, V. A.; Hueglin, C.; et al. *Science* **2009**, *326*, 1525–1529.
- (18) Zaveri, R. A.; Easter, R. C.; Shilling, J.; Seinfeld, J. H. *Atmos. Chem. Phys.* **2014**, *14*, 5153–5181.
- (19) Shiraiwa, M.; Seinfeld, J. H. *Geophys. Res. Lett.* **2012**, *39*, L24801.
- (20) Zaveri, R. A.; Shilling, J.; Zelenyuk, A.; Liu, J.; Bell, D. M.; D'Ambro, E. L.; Gaston, C. J.; Thornton, J. A.; Laskin, A.; Lin, P.; Wilson, J.; Easter, R. C.; Wang, J.; Bertram, A. K.; Martin, S. T.; Seinfeld, J. H.; Worsnop, D. R. *Environ. Sci. Technol.* **2018**, *52*, 1191–1199.
- (21) Boucher, O. D.; Randall, D.; Artaxo, P.; Bretherton, C.; Feingod, G.; Forster, P.; Kerminen, V. M.; Kondo, Y.; Liao, H.; Lohmann, U.; Rasch, P.; Sathesh, S. K.; Sherwood, S.; Stevens, B.; Zhang, X. Y. *Clouds and Aerosols. Climate Change 2013: The Physical Science Basis. Contribution of Working Group I to the Fifth Assessment Report of the Intergovernmental Panel on Climate Change*; Cambridge University Press: Cambridge, United Kingdom, 2013.
- (22) Reid, J. P.; Bertram, A. K.; Topping, D.; Laskin, A.; Martin, S. T.; Petters, M. D.; Pope, F.; Rovelli, G. *Nat. Commun.* **2018**, *9*, 56, 1–14.
- (23) Rudich, Y. *Chem. Rev.* **2003**, *103*, 5097–5124.
- (24) Rudich, Y.; Donahue, N. M.; Mentel, T. F. *Annu. Rev. Phys. Chem.* **2007**, *58*, 321–352.
- (25) Lack, D.; Langridge, J.; Bahreini, R.; Cappa, C. D.; Middlebrook, A. M.; Schwarz, J. P. *Proc. Natl. Acad. Sci. U. S. A.* **2012**, *109*, 14802–14807.
- (26) Huffman, J. A.; Docherty, K. S.; Mohr, C.; Cubison, M. J.; Ulbrich, I. M.; Ziemann, P. J.; Onasch, T. B.; Jimenez, J. L. *Environ. Sci. Technol.* **2009**, *43*, 5351–5357.
- (27) Kolesar, K. R.; Li, Z.; Wilson, K. R.; Cappa, C. D. *Environ. Sci. Technol.* **2015**, *49*, 12242–12252.
- (28) An, W. J.; Pathak, R. K.; Lee, B.-H.; Pandis, S. N. *J. Aerosol Sci.* **2007**, *38*, 305–314.
- (29) Vaden, T. D.; Imre, D.; Beranek, J.; Shrivastava, M.; Zelenyuk, A. *Proc. Natl. Acad. Sci. U. S. A.* **2011**, *108*, 2190–2195.
- (30) Cappa, C. D.; Jimenez, J. L. *Atmos. Chem. Phys.* **2010**, *10*, 5409–5424.
- (31) Hildebrandt, L.; Engelhart, G. J.; Mohr, C.; Kostenidou, E.; Lanz, V. A.; Bougiatioti, A.; DeCarlo, P. F.; Prevot, A. S. H.; Baltensperger, U.; Mihalopoulos, N.; Donahue, N. M.; Pandis, S. N. *Atmos. Chem. Phys.* **2010**, *10*, 4167–4186.
- (32) Pósfai, M.; Simonics, R.; Li, J.; Hobbs, P. V.; Buseck, P. R. *J. Geophys. Res.* **2003**, *108*, 8483.
- (33) Li, W.; Sun, Y. L.; Xu, L.; Shi, Z.; Riemer, N.; Sun, Y.; Fu, P.; Zhang, J.; Lin, Y.; Wang, X.; Shao, L.; Chen, J.; Zhang, X.; Wang, Z.; Wang, W. *J. Geophys. Res. Atmos.* **2016**, *121*, 13784–13798.
- (34) Xu, L.; Liu, L.; Zhang, J.; Zhang, Y.; Ren, Y.; Wang, X.; Li, W. *Atmosphere* **2017**, *8*, 47.
- (35) Simonsen, S. B.; Chorkendorff, I.; Dahl, S.; Skoglundh, M.; Sehested, J.; Helveg, S. *J. Am. Chem. Soc.* **2010**, *132*, 7968–7975.
- (36) Asoro, M. A.; Kovar, D.; Ferreira, P. J. *Chem. Commun.* **2014**, *50*, 4835–4838.
- (37) Kovarik, L.; Bowden, M.; Genc, A.; Szanyi, J.; Peden, C. H. F.; Kwak, J. H. *J. Phys. Chem. C* **2014**, *118*, 18051–18058.
- (38) Stach, E. A.; Pauzauskie, P. J.; Kuykendall, T.; Goldberger, J.; He, R.; Yang, P. *Nano Lett.* **2003**, *3*, 867–869.
- (39) Asoro, M. A.; Kovar, D.; Ferreira, P. J. *ACS Nano* **2013**, *7*, 7844–7852.
- (40) Adachi, K.; Sedlacek, A. J.; Kleinman, L.; Chand, D.; Hubbe, J. M.; Buseck, P. R. *Aerosol Sci. Technol.* **2018**, *52*, 46–56.
- (41) Vendelbo, S. B.; Kooyman, P. J.; Creemer, J. F.; Morana, B.; Mele, L.; Dona, P.; Nelissen, B. J.; Helveg, S. *Ultramicroscopy* **2013**, *133*, 72–79.
- (42) Picher, M.; Mazzucco, S.; Blankenship, S.; Sharma, R. *Ultramicroscopy* **2015**, *150*, 10–15.
- (43) Lundt, N.; Kelly, S. T.; Rodel, T.; Remez, B.; Schwartzberg, A. M.; Ceballos, A.; Baldasseroni, C.; Anastasi, P. A. F.; Cox, M.; Hellman, F.; Leone, S. R.; Gilles, M. K. *Rev. Sci. Instrum.* **2013**, *84*, 104906.
- (44) Winterstein, J. P.; Lin, P. A.; Sharma, R. *Microsc. Microanal.* **2015**, *21*, 1622–1628.
- (45) Veghte, D. P.; Bittner, D. R.; Freedman, M. A. *Anal. Chem.* **2014**, *86*, 2436–2442.
- (46) Fraund, M.; Pham, D. Q.; Bonanno, D.; Harder, T. H.; Wang, B.; Brito, J.; de Sa, S. S.; Carbone, S.; China, S.; Artaxo, P.; Martin, S. T.; Pohlker, C.; Andreae, M.; Laskin, A.; Gilles, M. K.; Moffet, R. C. *Atmosphere* **2017**, *8*, 173.
- (47) Stein, A. F.; Draxler, R. R.; Rolph, G. D.; Stunder, B. J. B.; Cohen, M. D.; Ngan, F. *Bull. Am. Meteorol. Soc.* **2015**, *96*, 2059–2077.
- (48) Milazzo, A.-C.; Moldovan, G.; Lanman, J.; Jin, L.; Bouwer, J. C.; Klienfelder, S.; Peltier, S. T.; Ellisman, M. H.; Kirkland, A. I.; Xuong, N.-H. *Ultramicroscopy* **2010**, *110*, 741–744.
- (49) Hopkins, R. J.; Tivanski, A. V.; Marten, B. D.; Gilles, M. K. *J. Aerosol Sci.* **2007**, *38*, 573–591.
- (50) Moffet, R. C.; Henn, T. R.; Tivanski, A. V.; Hopkins, R. J.; Desyaterik, Y.; Kilcoyne, A. L. D.; Tylicszak, T.; Fast, J.; Barnard, J.; Shutthanandan, V.; Cliff, S. S.; Perry, K. D.; Laskin, A.; Gilles, M. K. *Atmos. Chem. Phys.* **2010**, *10*, 961–976.
- (51) Moffet, R. C.; Tivanski, A. V.; Gilles, M. K. *Scanning x-ray transmission microscopy: applications in atmospheric microscopy. Fundamentals and Applications in Aerosol Spectroscopy*; Taylor and Francis Books: New York, 2010.
- (52) Allard, L. F.; Bigelow, W. C.; Jose-Yacamán, M.; Nackashi, D. P.; Damiano, J.; Mick, S. *Microsc. Res. Tech.* **2009**, *72*, 208–215.
- (53) Zhang, Z.; Su, D. *Ultramicroscopy* **2009**, *109*, 766–774.
- (54) Haynes, W. M. *CRC Handbook of Chemistry and Physics*, 95th ed.; CRC Press, Taylor & Francis Group: Boca Raton, FL, 2014.
- (55) Oja, V.; Suuberg, E. M. *J. Chem. Eng. Data* **1999**, *44*, 26–29.
- (56) Zimm, B. H.; Mayer, J. E. *J. Chem. Phys.* **1944**, *12*, 362–369.
- (57) Bernard, S.; Beyssac, O.; Benzerara, K.; Findling, N.; Tzvetkov, G.; Brown, G. E. *Carbon* **2010**, *48*, 2506–2516.
- (58) Keiluweit, M.; Nico, P. S.; Johnson, M. G.; Kleber, M. *Environ. Sci. Technol.* **2010**, *44*, 1247–1253.
- (59) Veghte, D. P.; China, S.; Weis, J.; Kovarik, L.; Gilles, M. K.; Laskin, A. *ACS Earth Space Chem.* **2017**, *1*, 511–521.